METABOLISM

Molecular alterations in the extracellular matrix in the brains of newborns with congenital Zika syndrome

Renato S. Aguiar[1,2]*, Fabio Pohl[3]*, Guilherme L. Morais[4]*, Fabio C. S. Nogueira[5,6]*, Joseane B. Carvalho[4]*, Letícia Guida[7]*, Luis W. P. Arge[4], Adriana Melo[8], Maria E. L. Moreira[7], Daniela P. Cunha[7], Leonardo Gomes[7], Elyzabeth A. Portari[7], Erika Velasquez[5], Rafael D. Melani[5], Paula Pezzuto[1], Fernanda L. de Castro[1], Victor E. V. Geddes[1], Alexandra L. Gerber[4], Girlene S. Azevedo[8], Bruno L. Schamber-Reis[9], Alessandro L. Gonçalves[1], Inácio Junqueira-de-Azevedo[10], Milton Y. Nishiyama Jr.[10], Paulo L. Ho[11], Alessandra S. Schanoski[11], Viviane Schuch[3], Amilcar Tanuri[1], Leila Chimelli[12†], Zilton F. M. Vasconcelos[7†], Gilberto B. Domont[5†], Ana T. R. Vasconcelos[4†], Helder I. Nakaya[3,13†]

Zika virus (ZIKV) infection during pregnancy can cause a set of severe abnormalities in the fetus known as congenital Zika syndrome (CZS). Experiments with animal models and in vitro systems have substantially contributed to our understanding of the pathophysiology of ZIKV infection. Here, to investigate the molecular basis of CZS in humans, we used a systems biology approach to integrate transcriptomic, proteomic, and genomic data from the postmortem brains of neonates with CZS. We observed that collagens were greatly reduced in expression in CZS brains at both the RNA and protein levels and that neonates with CZS had several single-nucleotide polymorphisms in collagen-encoding genes that are associated with osteogenesis imperfecta and arthrogryposis. These findings were validated by immunohistochemistry and comparative analysis of collagen abundance in ZIKV-infected and un-infected samples. In addition, we showed a ZIKV-dependent increase in the expression of cell adhesion factors that are essential for neurite outgrowth and axon guidance, findings that are consistent with the neuronal migration defects observed in CZS. Together, these findings provide insights into the underlying molecular alterations in the ZIKV-infected brain and reveal host genes associated with CZS susceptibility.

INTRODUCTION

Zika virus (ZIKV) infection during pregnancy is associated with several neurological problems in the fetus (*1*, *2*). Together, this set of abnormalities is known as congenital Zika syndrome (CZS) and can involve microcephaly, brain calcifications, ventriculomegaly, and cortical malformations due to migration disorders, including agyria/lissencephaly, congenital contractures, and ocular abnormalities (*1*, *3*, *4*). In adults, the most common symptoms of ZIKV infection are fever, rash, arthralgia, conjunctivitis, and headache (*5*). Although most pregnant women exposed to ZIKV give birth to healthy babies, 0.3 to 15% of cases develop CZS (*6*). The frequency of infant deaths (miscarriages and perinatal deaths) is low (~1% of CZS), and most of them present intrauterine akinesia syndrome (arthrogryposis) (*7*). Several studies in vitro and with brain organoids and neurospheres demonstrated that ZIKV directly infects human neural progenitor cells (hNPCs) (*8*), impairs cortical development (*9*), affects neuron migration and, thus, brain size (*10*), and promotes brain malformation (*11*). Nevertheless, the molecular basis of CZS and the susceptibility genes associated with the most severe cases in human newborns remain unknown.

Systems biology approaches have been successfully applied to reveal the molecular mechanisms associated with viral infection and vaccination (*12*, *13*). By integrating different types of omics data, systems biology provides a global overview of the network of genes, transcripts, proteins, and metabolites involved with a biological condition or perturbation (*14*). When applied to human infectious diseases, systems biology could provide critical insights into the complex interplay between pathogen and host, thereby leading to new potential intervention strategies.

In this study, we generated genomic, transcriptomic, and proteomic data from the blood and postmortem brain samples of eight neonates with confirmed ZIKV infection during pregnancy and with no congenital genetic diseases or another fetal infection that can cause congenital malformations [STORCH (syphilis, cytomegalovirus, herpes virus 1/2, *Toxoplasma gondii*, and rubella virus)]. After three-layer omics data integration, we highlighted the molecular pathways underlying neurological damage. Systems biology combined with histopathological analysis revealed that genes associated with matrix organization were substantially reduced in expression in the brains

[1]Departamento de Genética, Instituto de Biologia, Universidade Federal do Rio de Janeiro, Rio de Janeiro, Brazil. [2]Departamento de Biologia Geral, Instituto de Ciências Biológicas, Universidade Federal de Minas Gerais, Belo Horizonte, Brazil. [3]Department of Clinical and Toxicological Analyses, School of Pharmaceutical Sciences, University of São Paulo, São Paulo, Brazil. [4]National Laboratory of Scientific Computation, LNCC/MCTI, Petrópolis, Brazil. [5]Proteomics Unit, Department of Biochemistry, Institute of Chemistry, Federal University of Rio de Janeiro, Rio de Janeiro, Brazil. [6]Laboratory of Proteomics, LADETEC, Institute of Chemistry, Federal University of Rio de Janeiro, Rio de Janeiro, Brazil. [7]Fernandes Figueira Institute, Fiocruz, Rio de Janeiro, Brazil. [8]Instituto de Pesquisa Professor Amorim Neto, Campina Grande, Paraíba, Brazil. [9]Faculdade de Ciências Médicas de Campina Grande, Núcleo de Genética Médica, Centro Universitário UniFacisa, Campina Grande, Paraíba, Brazil. [10]Special Laboratory for Applied Toxinology, Butantan Institute, São Paulo, Brazil. [11]Bacteriology Laboratory, Butantan Institute, São Paulo, Brazil. [12]Laboratório de Neuropatologia, Instituto Estadual do Cérebro, Rio de Janeiro, Brazil. [13]Scientific Platform Pasteur-USP, São Paulo, Brazil.
*These authors contributed equally to this work.
†Corresponding author. Email: hnakaya@usp.br (H.I.N.); atrv@lncc.br (A.T.R.V.); gilbertodomont@gmail.com (G.B.D.); zilton.vasconcelos@iff.fiocruz.br (Z.F.M.V.); chimelli@hucff.ufrj.br (L.C.)

of neonates with CZS, which may explain the neuronal migration disorders and microcephaly attributed to ZIKV infection.

RESULTS
Neonates with severe CZS
From October 2015 to July 2016, we followed a group of pregnant women with symptoms of ZIKV exposure at distinct weeks of gestation and from two endemic areas in Brazil: the northeast (Campina Grande, Paraíba state) and southeast (Rio de Janeiro, Rio de Janeiro state) regions. During this period, we enrolled pregnant women who were referred to public health care with a history of rash or fetus with central nervous system (CNS) abnormality confirmed by ultrasonography or magnetic resonance imaging (MRI), as well as postnatal physical examination suggestive of microcephaly. We focused on eight neonates that had died in the first 48 hours postpartum with severe arthrogryposis (Fig. 1A). The ZIKV genome was detected in all cases during pregnancy by reverse transcription polymerase chain reaction (RT-PCR) analysis of clinical samples from mothers and neonates, such as urine, plasma, amniotic fluid, placenta, and umbilical cord. We also detected the virus genome through RT-PCR and in situ hybridization (ISH) analyses of postmortem fetal tissues (Fig. 1B). Other microcephaly causes, including congenital genetic diseases, infection with arboviruses that circulate in the same area (dengue and chikungunya), and teratogenic pathogens (STORCH), were all excluded (table S1).

Five of eight cases of CZS showed ZIKV exposition symptoms in the first trimester of pregnancy, corroborating other reports (15, 16) that describe an increasing risk of microcephaly at the beginning of gestation (Fig. 1A). Microcephaly was observed in the early gestation weeks through ultrasonography in all cases (Fig. 1C). However, the cephalic perimeter at birth was considered to be normal (>32 cm) in most of the neonates due to severe ventriculomegaly or obstructive hydrocephalus. The brain usually collapsed after removal of the skull during autopsy, which revealed tiny brains in all cases (on average 66 g; ranging from 7 to 180 g). A detailed neuropathological description of all cases has been previously reported (10).

Those brains with greater viral load (lower cycle threshold or Ct values) exhibited the most destructive patterns of CNS structures (Fig. 1B and table S1). Macroscopic observations showed thick-

ened and congested leptomeninges, very thin parenchyma and corpus callosum, and asymmetric ventriculomegaly (Fig. 1D). Shallow sulci or agyria was prevalent in all cases (Fig. 1D). The hippocampus, basal ganglia, and thalami were usually not well identified and malformed. Cerebellar hypoplasia was observed in all cases, with an irregular cortical surface, and calcification foci were detected macroscopically. The brainstem was deformed and hypoplastic in most of the cases.

The histopathological analysis confirmed the migration disturbances represented by abnormal immature cell clusters along the white matter and over pia mater (table S2). An intense immune response to cell injury was observed in all cases as demonstrated by the gliosis and inflammatory infiltrate (T lymphocytes and histiocytes) in the meninges, cerebral hemispheres, and spinal cord (tables S1 and S2). Reduction in the descending motor fibers was
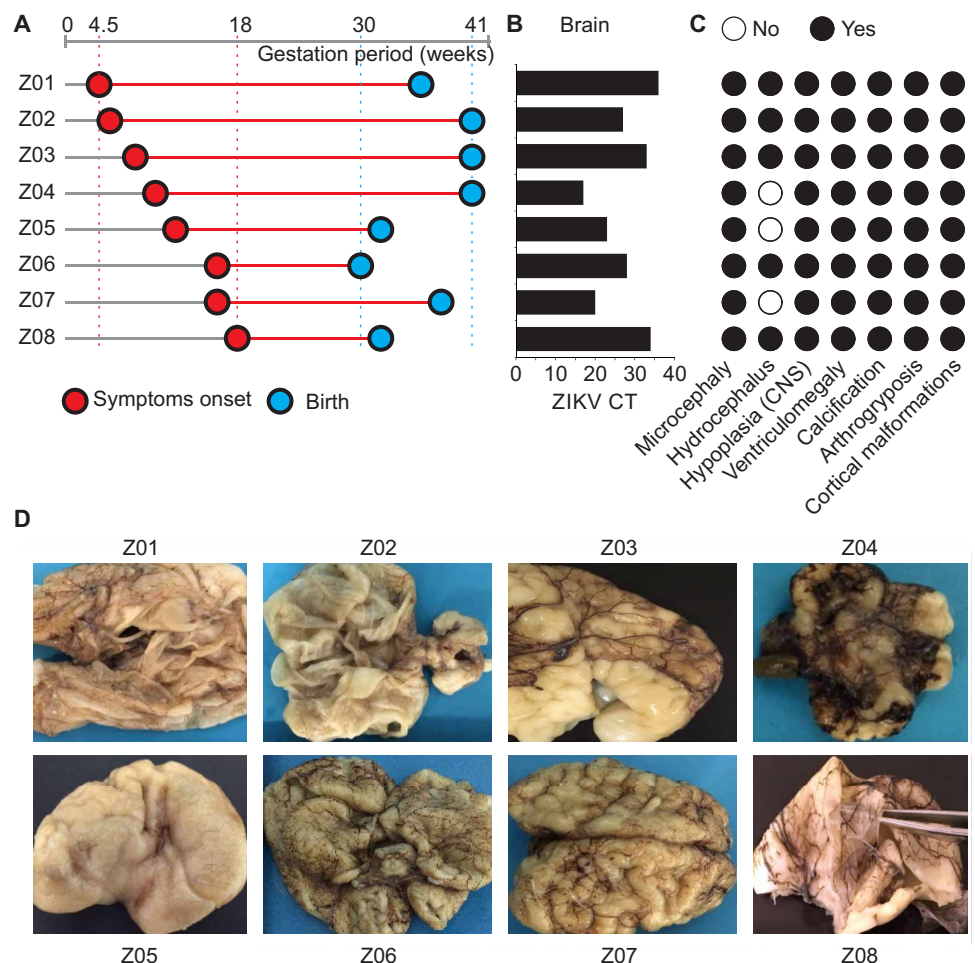
Fig. 1. Clinical diagnoses and brain damage of deceased neonates with CZS. (A) Gestational timeline for the eight ($N = 8$) neonates (Z01 to Z08) with CZS. The symptoms included fever, exanthema, arthralgia, conjunctivitis, and headache in pregnant women during gestation. (B) ZIKV genome detection by RT-PCR analysis of samples from postmortem brains ($N = 8$) expressed in Ct values. (C) Lesions in the CNS of neonates ($N = 8$) with CZS were investigated by prenatal ultrasound and MRI examinations. At birth, only three cases (Z04, Z05, and Z07) had microcephaly. The other cases had normal or enlarged cephalic perimeter due to obstructive hydrocephalus. Hypoplasia was found in the cerebellum and the brainstem. Cortical malformations were due to disrupted neuronal migration (agyria, polymicrogyria, or lissencephaly). (D) Brains from the autopsies showing congested leptomeninges and various degrees of lesions, including collapse due to hydrocephalus and small brains with few gyri or agyria. The numbers of the ZIKV cases are depicted as presented in table S1.

also observed. The histopathological analysis also displayed a loss of motor nerve cells in the spinal cord, as well as atrophy of the skeletal muscle. These findings could explain the intrauterine akinesia and consequent arthrogryposis observed in all cases (tables S1 and S2).

Transcriptome and proteome analyses of CZS brains

We used high-throughput sequencing and mass spectrometry (MS) technologies to assess the changes in the transcriptome and proteome in the frontal cortex of CZS brains (Z03, Z05, and Z08 from Fig. 1) compared with the control brain (Edwards syndrome). Differential expression analysis revealed 509 genes associated with CZS, of which 228 genes were increased in expression and 281 genes were reduced in expression in ZIKV-infected neonates (fig. S1A and table S3). Among the Reactome pathways enriched with genes with increased expression, we found "unblocking of NMDA receptor, glutamate binding, and activation" and "glutamate neurotransmitter release cycle" (fig. S1A and table S3). These findings support our previous in vitro work, showing that blockage of the NMDA (N-methyl-D-aspartate) receptor prevents neuronal death induced by ZIKV infection (17). Among the pathways enriched with genes that were decreased in expression, we found those involved in collagen formation, glucose metabolism, signaling by transforming growth factor–β (TGF-β) receptor complex, class I major histocompatibility complex (MHC)–mediated antigen processing and presentation, and amyloid fiber formation (fig. S1B). The genes that were decreased in expression suggest that ZIKV infection could affect immune-response pathways, cellular metabolism, and the very formation of connective tissue in the brain.

The expression of genes associated with cell adhesion, which are essential for neuronal migration and the recruitment of immune cells including neural cell adhesion molecule (NCAM) receptors, was increased in the CZS brains, which corroborates the migration disturbance and inflammatory infiltration events (CD8^{+} T cells and CD68^{+} histiocytes) observed in the histopathological analysis (table S3). Collagen-encoding genes (including *COL1A1*, *COL1A2*, *COL3A1*, *COL5A1*, *COL5A2*, *COL6A3*, *COL12A1*, and *COL14A1*), which are essential for the development of the brain and the blood-brain barrier (18), were decreased in expression in the CZS brains.

We subsequently investigated protein abundances in CZS brains compared with those in the brain of the ZIKV-negative control. The proteomic analysis identified 252 and 110 proteins that were increased or decreased in abundance in CZS brains, respectively (Fig. 2A and table S4). Furthermore, a set of proteins were exclusively detected either in brains with CZS (714 proteins) or in the ZIKV-negative control brain (79 proteins) (Fig. 2A and table S4). Similar to the transcriptomic analysis, those proteins that were increased in abundance were enriched for pathways related to "glucose metabolism" and "L1CAM interactions," whereas those proteins that were reduced in abundance were enriched for "extracellular matrix (ECM) organization" and "collagen formation" (Fig. 2B and table S4). Among the proteins that were less abundant in the brains of all three neonates with CZS than in the control brain were COL1A1, COL1A2, PPIB, SERPINH1, and OGN. Whereas PPIB is instrumental in collagen trimerization, SERPINH1 is critical to collagen biosynthesis (19). In addition, the functions of OGN in the ECM are related to collagen fibrillogenesis, cell proliferation, and development, as well as osteoblast differentiation and bone development (20).

The prefrontal cortex is a heterogeneous tissue composed of several cell types that interact with one another in a complex manner.
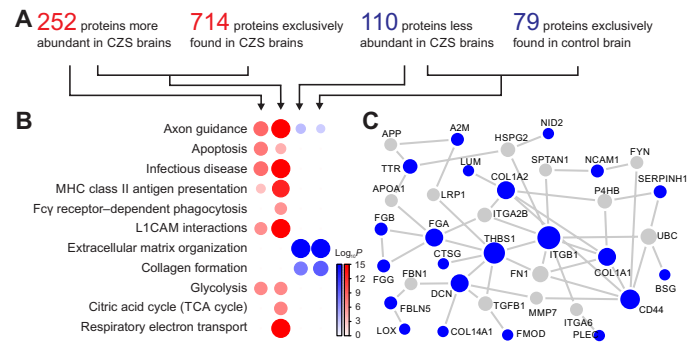

Fig. 2. Proteins related to CZS and microcephaly. (**A**) The number of differentially expressed proteins that were increased (red) or decreased (blue) in abundance in CZS brains ($N = 3$) compared with those in the ZIKV-negative control brain in the prefrontal cortex. Proteins with an adjusted P value of <0.05 as determined by limma moderated t test were considered to be differentially abundant. Proteins found either only in CZS brains or only in the control brain were considered to be exclusively expressed proteins. (**B**) Enrichment of functional pathways for proteins found in CZS brains ($N = 3$). Red represents the proteins that were increased in abundance, whereas blue represents the proteins that were decreased in abundance. The adjusted P value ($-\log_{10}$) of overrepresentation analysis is indicated by color intensity and circle size. (**C**) Protein-protein interactions for proteins that were decreased in abundance in CZS brains. Blue nodes indicate the proteins observed to be reduced in abundance, whereas the gray nodes indicate additional proteins. The circle size represents the node degree. TCA, tricarboxylic acid.

Our results reflect alterations in the frequencies of specific cell types within the tissue, as well as the transcriptional changes within those cells. Therefore, assessing the transcriptome changes in isolated primary neurons or in hNPCs through in vitro assays may represent an incomplete picture of the effect of ZIKV infection on the human brain. We compared our transcriptome results with the ZIKV-related genes reported in previously published in vitro RNA sequencing (RNA-seq) studies, which used hNPCs, neural crest cells, fetal neural stem cells, and peripheral neurons infected with either the Asian strain (FSS12025, PRVABC59, and Mex1-7) or the African strain (MR766) of ZIKV (fig. S2A). Ten and 17 genes were increased or decreased in expression, respectively, in all comparisons. These included genes encoding the proliferation marker Ki-67, the transcription factor associated with cell cycle E2F2, the growth factor VEGFA (vascular endothelial growth factor A), which induces the permeabilization of blood vessels, and the cysteine and glutamate transporter SLC7A11 (fig. S2B). The gene signature of in vitro ZIKV infection was defined as genes that were either increased or decreased in expression when compared with uninfected cells in at least four comparisons (fig. S2B). Only a small fraction of the differentially expressed genes (DEGs) found in our postmortem samples were present in the in vitro ZIKV infection gene signature, indicating that our postmortem gene signature is distinct (fig. S2C). Furthermore, in vitro experiments found genes consistently associated with ZIKV infection, such as *MKI67*, *COL1A2*, *SCL7A11*, and *SMC4*, which were also detected in the postmortem samples (fig. S2C). We also compared our transcriptome and proteome results with the gene and protein signatures of human neurospheres infected with the Brazilian strain of ZIKV (BR_ZIKV_AB_ES) as described by Garcez *et al.* (11). Only a very small fraction of genes (fig. S2D) and proteins (fig. S2E) were shared by the in vitro experiments and our postmortem study.

Protein-protein interaction (PPI) data obtained from the Search Tool for the Retrieval of Interacting Genes/Proteins (STRING) database were used to assess the interacting proteins related to the brain's connective tissue (Fig. 2C). The interactome showed the same pattern of reduction in the abundance of essential protein hubs involved in collagen formation (COL1A1 and COL1A2) and adhesive glycoproteins that mediate cell-to-cell and cell-to-matrix interactions (ITGA2B, NCAM, FNB, IGB1, and THBS1). LOX, whose mRNA and protein were both reduced as determined by transcriptome and proteome analyses, plays a key role in cross-linking fibers of collagen and elastin. The reduction in collagen pathways in the brain endothelia could partially explain the vascular problems and ischemia events observed in CZS neonates. The interactome showed the modulation of fibrinogen components (FGA, FGB, and FGG), which are components of blood clots and are formed after vascular injury. These findings relate to the intense blood-congested leptomeninges found in the CZS brains (Figs. 1D and 2C).

We subsequently cross-referenced the lists of genes and proteins that were differentially expressed in CZS compared with the negative control and found, respectively, 12 and 23 genes and their protein products that were increased or decreased in expression (Fig. 3A). The functions of several of these genes could provide insights into ZIKV neuropathogenesis. For example, *NCAM1* is essential for neurite outgrowth, *COL1A1* and *COL1A2* encode the α1 and α2 chains of collagen type I, and the *PRDX2* product peroxiredoxin 2 regulates the antiviral activity of T cells (Fig. 3A). For *TTR* and *AGT* genes, however, their mRNA abundances were greater in the CZS samples than in the control, whereas the abundances of the corresponding proteins were reduced in CZS. Similarly, eight genes were decreased in expression, but their encoding proteins were increased in abundance. These inverted patterns between mRNAs and proteins could partially be due to posttranscriptional regulation mechanisms that include microRNAs (miRNAs). Thus, we checked whether genes whose mRNAs, but not protein products, were increased in abundance were known miRNA targets. Our in silico approach predicted that eight miRNAs were induced upon infection and possibly involved regulation of genes related to CZS (Fig. 3B). Among them, mir-17-5p is induced by flavivirus infections, including ZIKV infection of astrocytes (*21*).

Rather than being differentially abundant, some proteins were exclusively detected either in brain samples with CZS or in the ZIKV-negative control brain. After including those, we found that 99 proteins, whose abundance was changed or that were uniquely detected in CZS or control samples (Fig. 3A), were encoded by genes that
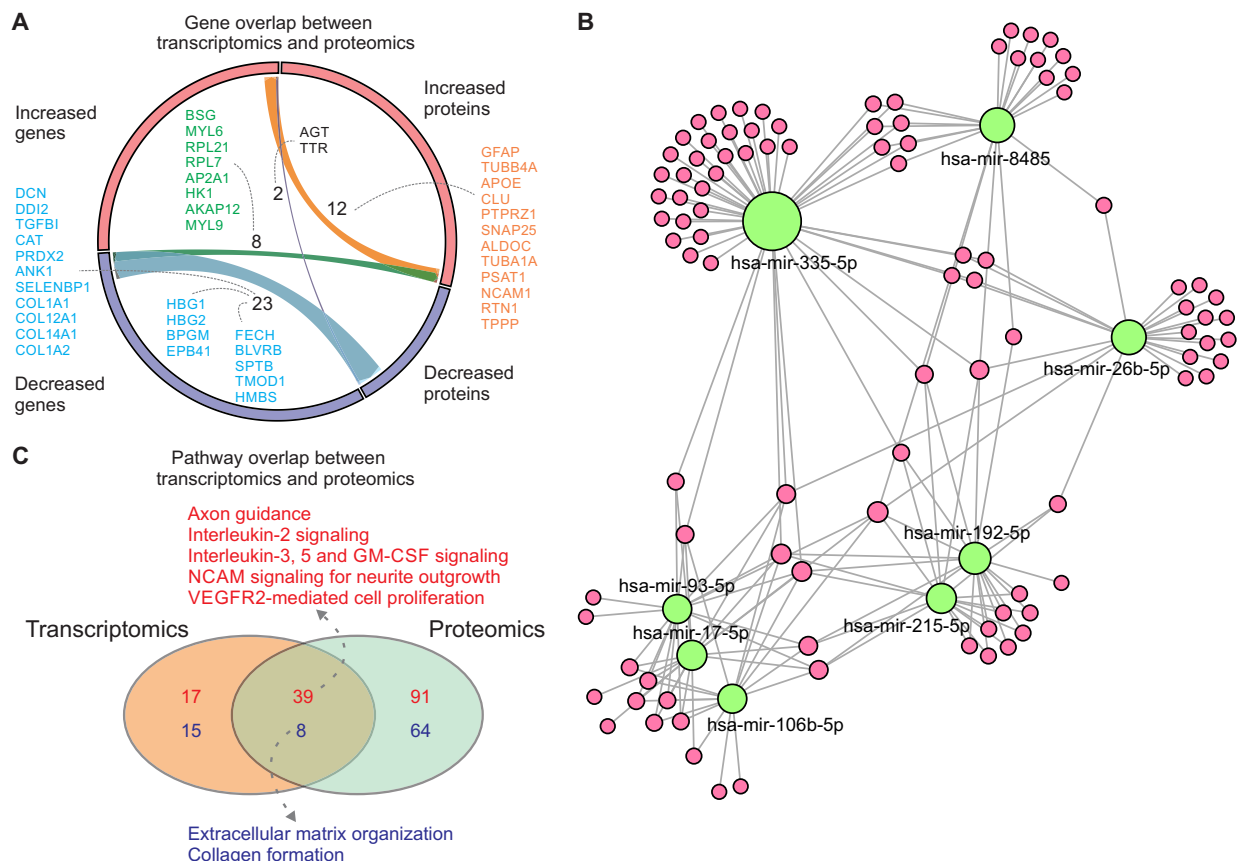

Fig. 3. Transcriptomics and proteomics interplay in CZS. (**A**) The overlap between differentially expressed genes (DEGs) and differentially expressed proteins (DEPs) in CZS brains (*N* = 3) compared with those in ZIKV-negative control brain in the prefrontal cortex. The fractions of genes and proteins that were increased in expression or abundance are represented by orange and violet bars, respectively. The links represent the overlap between both DEGs and DEPs, and the dashed lines indicate overlapped genes. (**B**) miRNAs predicted to regulate the genes that were increased in expression in the transcriptomic dataset but whose products were not increased in abundance in the proteomics dataset. (**C**) Pathways enriched in the transcriptomics and proteomics datasets. Numbers in red and blue indicate pathways enriched with genes that were increased or decreased in expression, respectively. Dashed lines indicate common pathways. GM-CSF, granulocyte-macrophage colony-stimulating factor.

were differentially expressed in CZS compared with control (tables S3 and S4). These included LOX, PSMF1, NCAN, TNR, and NRCAM (neuronal cell adhesion molecule), which are associated with cross-linking of collagen and elastin, processing of class I MHC peptides, modulation of cell adhesion and migration, and neuronal cell adhesion.

We also integrated our transcriptomics and proteomics data at the pathway level. Gene set enrichment analysis was performed using the mean fold change between CZS and control brains as ranks and the Reactome pathways as gene sets. The overlap between the transcriptomics and proteomics at pathway level, with 47 pathways statistically significantly enriched for both layers of information (Fig. 3C), was greater than the overlap obtained using the gene and protein levels (Fig. 3A). Furthermore, down-regulated pathways were related to ECM organization and collagen formation and are suggestive of a central role of collagen in CZS outcome.

Genetic variants associated with CZS
Whole-exome sequencing analysis identified several rare variants with potential deleterious functions in five neonates (Z01, Z02, Z04, Z06, and Z07 in Fig. 1). Combining variants that are presented in the same gene, we found that 23 genes had at least one single-nucleotide polymorphisms (SNPs) in all five neonates (Fig. 4A and table S5). Variants in genes and in affected protein domains associated with ECM organization (collagen-encoding genes, *FBN2*, *FBN3*, and *FN1*) (Fig. 4B and table S5), as well as CNS development (*PTPRZ1*), the immune system (*C7*, *C8A*, *IL4R*, *IL7*, *IRF3*, and *TLR2*), muscular contraction and arthrogryposis (*PIEZO2*, *RYR1*, and *TTN*), and Notch

and Wnt signaling pathways (*NOTCH3*, *NOTCH4*, and *VANGL1*), were also found (table S5). We also found variants in immune-related genes with splice-donor, missense, or stop-gain effects that were deleterious or that cause protein damage, especially in important protein domains, and with minor allele frequency (MAF) ranging from <0.01 to 5% (table S5).

Integration of three omics data types
The three layers of biological information were ultimately integrated into a network containing the gene variants and the RNAs and proteins that were differentially expressed in CZS cases (Fig. 5). Only three genes appeared to be associated with CZS in all of these layers: *COL1A1*, *COL12A1*, and *PTPRZ1* (Fig. 5A). The former two collagen-encoding genes are related to ECM organization. The latter gene *PTPRZ1* is instrumental to the differentiation of oligodendrocytes (*22*) and is associated with schizophrenia (*23*). In total, there were 1628 genes associated with CZS at either the genomic, transcriptomic, or proteomic level. PPI data were used to construct a network with 341 of these gene products (Fig. 5B). Network analysis revealed several modules associated with proteasome-mediated degradation, axon guidance, the fibroblast growth factor signaling pathway, and Parkinson's disease (Fig. 5B).

A more stringent analysis was performed including only the 64 genes that were identified as being associated with CZS in at least two omics analyses (Fig. 5A). Subsequently, the products of these genes were integrated into a PPI network (fig. S3). Several highly connected genes were observed—THBS1 promotes synaptogenesis
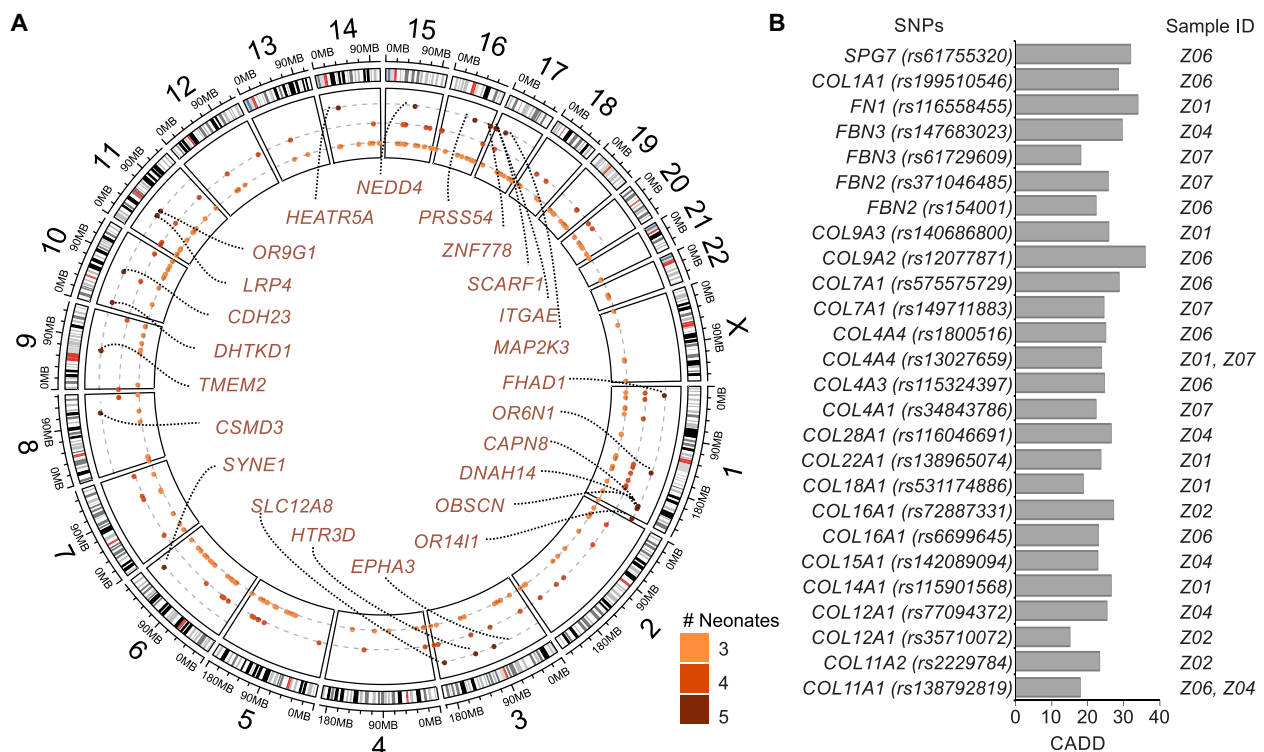
Fig. 4. SNPs in neonates with CZS. Five CZS cases (*N* = 5) were subjected to exome analysis. (**A**) Genomic map showing genes with SNPs (MAF < 0.05 and CADD > 15) in three or more neonates with CZS. The outermost layer represents the reference genome (GRCh38). In the middle layer, each row represents genes with at least one SNP in three to five neonates. Dark brown rows represent genes that contain variants in all five neonates. (**B**) List of the most deleterious SNPs found in genes encoding ECM components.
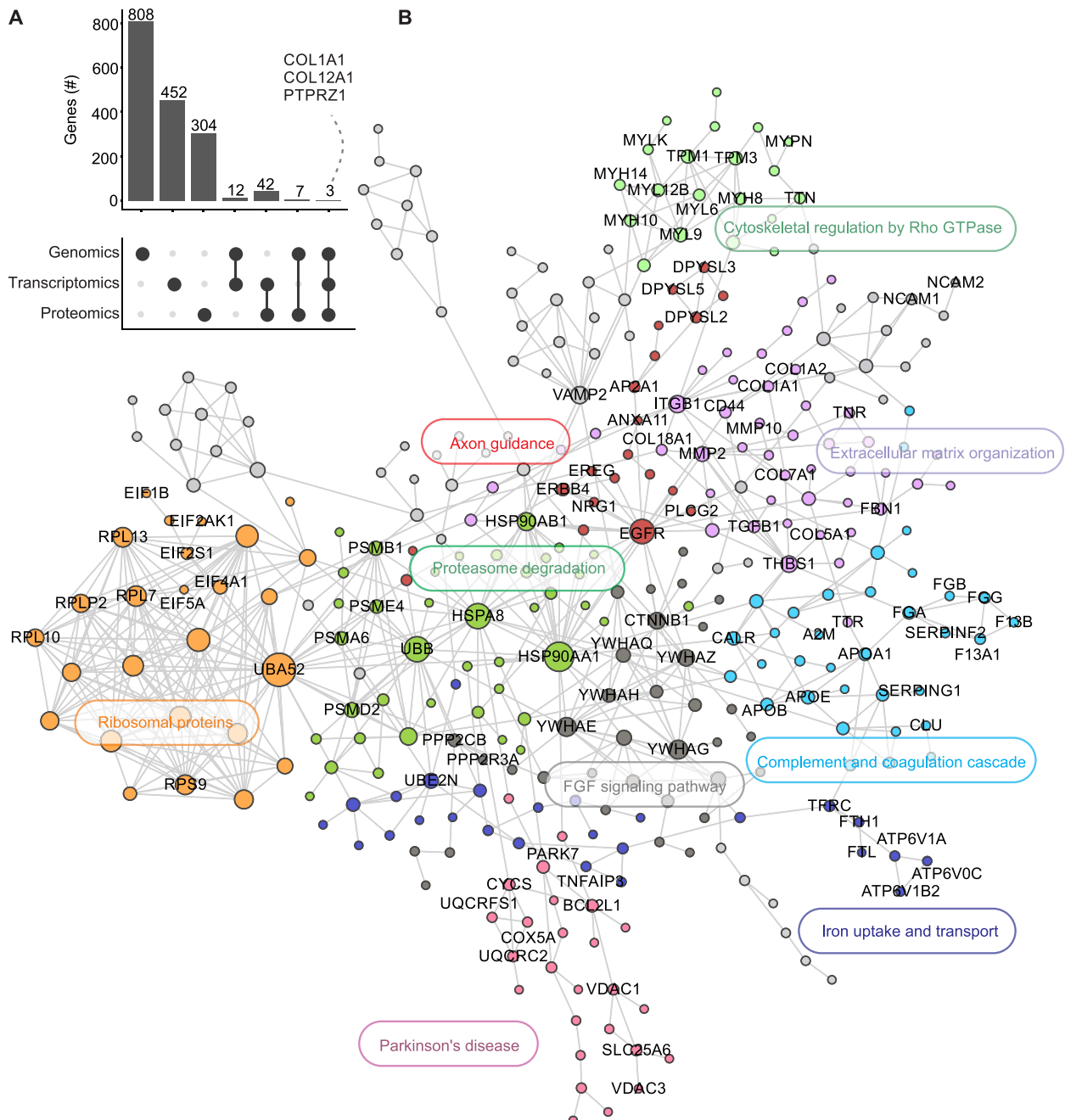
Fig. 5. Integration of three molecular layers in postmortem ZIKV-infected samples. (**A**) Intersections between the three layers of information (genomics, transcriptomics, and proteomics) derived from the analysis of CZS samples. Bottom: The point diagram represents the intersections between the indicated layers. Top: Bar graph shows the number of genes in each intersection. A dashed line indicates the genes present in all the layers. (**B**) The PPI network of proteins encoded by CZS-related genes, together with their cellular pathways. GTPase, guanosine triphosphatase.

(24), DCN is necessary for maintaining collagen fibrils (25), and CLU is associated with amyloid deposition in the brain (26).

Because all of the analyses indicate that collagen-encoding genes are decreased in expression in CZS brains, we performed a Gomori's trichrome staining for total collagen in CZS brains, as well as in a different set of ZIKV-negative control brains. We observed a reduction in the amount of collagen fibers in the CZS brains, particularly in the adventitia of the vessels, compared with that in the Zika-negative controls at the same gestational age. This reduction validated our transcriptome and proteome findings (Fig. 6A). Next, we assessed the presence of COL1A1 through immunostaining directly in the brain tissues from CZS cases relative to the controls, and we found that COL1A1 was less abundant in all of the CZS cases (Fig. 6B). This finding supported the role of collagen isoforms in the neuropathogenesis associated with ZIKV infection in the brain tissues (Fig. 6B).
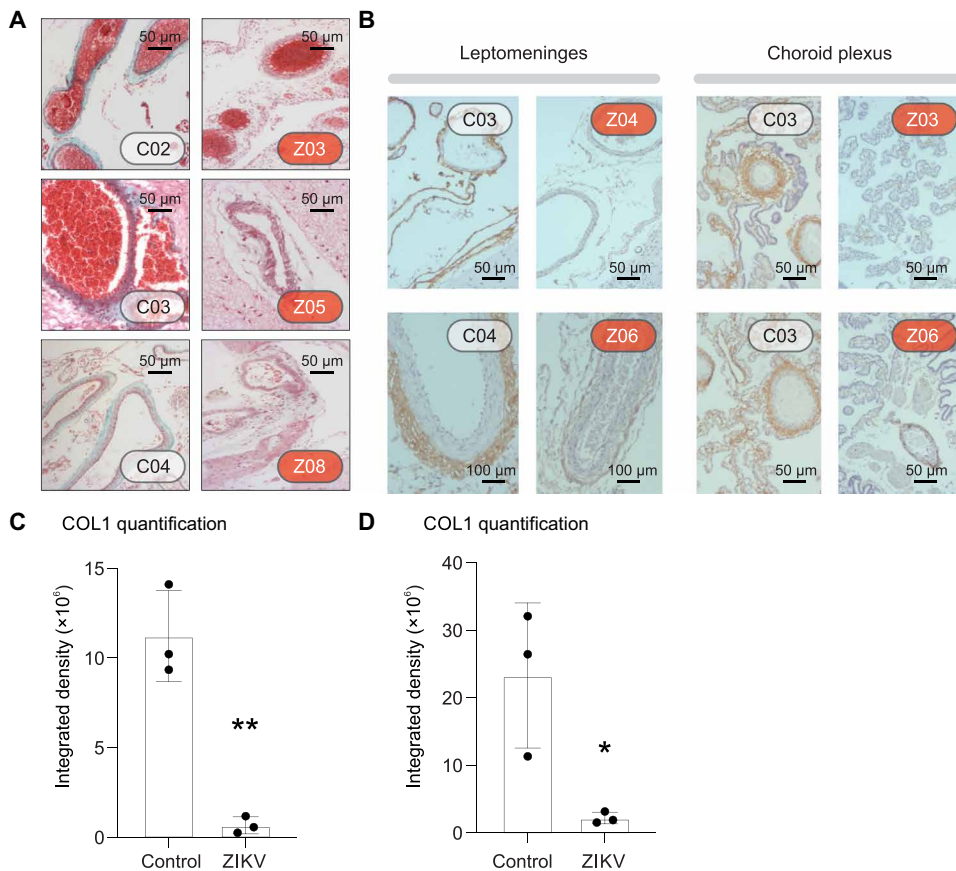
Fig. 6. The amount of collagen fibers in CZS cases is reduced compared with that in ZIKV-negative controls. (**A**) Histopathological analysis showing collage fibers in CZS brains ($N = 3$) and ZIKV-negative control brains at the same gestational age. Scale bars, 50 μm. (**B**) Immunohistochemical staining for collagen 1 in the leptomeninges and the choroid plexus of CZS brains ($N = 3$) and negative controls ($N = 2$), which are labeled as presented in tables S1 and S3. Scale bars, 50 μm. (**C** and **D**) Quantification of collagen 1 staining in the adventitia of the vessels from the leptomeninges of CZS samples compared with controls. (C) Total collagen quantification from the experiments shown in (A). (D) Specific collagen 1 quantification from the experiments shown in (B). The CZS cases ($N = 3$) are depicted as presented in table S1. Scale bars, 50 μm. *$P = 0.02$; **$P = 0.002$.

DISCUSSION

Our findings suggest that collagen-encoding genes and the ECM may play important roles in CZS. Reduced amounts of fibronectin and collagen IV increase the permeability of the blood-brain barrier (27). Once this barrier is transposed, ZIKV could reach developing neural progenitor cells and severely disrupt neural development. However, a more direct effect on fibroblast cells in the surrounding vasculature (28) cannot be excluded, and this effect could be a result of cell death or dysregulation of ECM production or tissue deposition. A relationship between the modulation of ECM-encoding gene expression and ZIKV was reported in an experimental monkey model during viral persistence in the CNS. Aid *et al.* (29) showed that viral loads and viral persistence were negatively correlated with ECM-encoding genes, including collagen-encoding genes. Experiments with animal models indicate that a deficiency in collagen compromises vessel resistance (30). Mutations in the genes encoding collagen IV and fibronectin result in impaired basement membranes and mesoderm defects, respectively (31). Moreover, mutations in *COL1A* and *COL4A1* cause defects in the basal membrane, resulting in a weakening of the brain vessels, arterial rupture, and ischemic stroke

(32, 33). Together with the effect on collagen isoforms, the decreased expression of *LOX*, whose product cross-links collagen fibers to elastin, could potentiate the vascularity deficiency. This could explain the blood congestion in the leptomeninges observed in all of the brain samples analyzed here. Specifically, glycine mutations affecting exon 49 of the *COL1A2* gene are associated with an increased risk of intracranial bleeding (34). Both collagen-encoding and *LOX* genes are induced in glioblastoma cells, and suppression of this pathway by ZIKV infection could explain the decreased angiogenesis and anticancer effects that several groups are exploring to treat glioblastoma with ZIKV-like particles (35–37). Moreover, the work of Ferraris *et al.* (38) showed that ZIKV infection might initiate early activation of the Notch pathway, resulting in the abnormal differentiation of neural progenitor cells, which is implicated in ZIKV-induced brain injury. Variants in the genes encoding NOTCH3 and NOTCH4 were found in two late neonates (38).

A caveat of our work is the fact that the transcriptome and proteome analyses were performed with frontal cortex tissues, which contain different CNS cells. Our histopathological analysis showed CD8^{+} T cell infiltrates and other CD3^{+} T cells in the cortex, reinforcing the contribution of immune cells in our expression analysis (10). However, the genes and pathways described here are consistent with previous transcriptome analysis performed with specific microglia and human neurospheres, which showed that ZIKV reprograms the adaptive immune response, RNA metabolism, adenosine triphosphate (ATP) production, glycolysis, and cell cycle pathways (11). However, we expanded this analysis to the brain architecture level and showed the modulation of collagen-encoding genes in the frontal cortex and blood vessels.

Mutations in the gene encoding type I collagen also affect the ECM by decreasing the amount of secreted collagen(s), impairing molecular and supramolecular assembly through the secretion of mutant collagen or by inducing endoplasmic reticulum stress and the unfolded protein response (39). Mutated *COL1A1* is also associated with osteogenesis imperfecta, a generalized disorder of connective tissues that resembles the observed arthrogryposis phenotype common to all cases included in this work (40). Mutations in *COL1A1/2* genes are associated with congenital brittle bones with the development of microcephaly and cataracts, as observed in the most severe cases of CZS (41). A dominant mutation in *COL12A1* is also related to joint laxity (42), a phenotype often found in ZIKV-infected children (43).

Cell-cell interactions are necessary for neuronal migration through the cortex layers during neurodevelopment (44). Members of the

L1CAM family of cell adhesion molecules are associated with neurite outgrowth and axon guidance (45). In ZIKV-infected brains, NCAM1 and NFASC were increased in abundance both at the RNA and protein levels. In addition, we found a rare variant in NRCAM gene located in the immunoglobulin-like domain. NRCAM is involved in various functions, including cell-cell recognition, cell surface receptors, muscle structure, and the immune system (46). These findings suggest that the aforementioned genes and proteins could be the molecular basis for neuronal migration defects already described by our group (10) and could lead to CNS structural defects and the reduction in the size of the cortical region observed in CZS newborns.

Among the pathways enriched in genes with increased expression in ZIKV-infected samples, we found genes related to glutamate neurotransmitter release cycle and unblocking of the NMDA receptor, glutamate binding, and activation. Previous experimental work revealed that NMDA receptor blockage has a protective effect on ZIKV-induced cell death (17). In addition, proteins associated with apoptosis were also increased in response to ZIKV infection. This finding is consistent with the increased cell death proposed to neural progenitor cell pool and revealed by experimental data (47).

Successful viral infection and disease must overcome the host immune response. Pleiotrophin (PTN) is a cytokine that modulates inflammation in the CNS (48). In addition, PTN inhibits protein tyrosine phosphatase zeta (PTPRZ1), which binds to developmental proteins, such as β-catenin (49). Our study showed that PTPRZ1 was increased in abundance at the mRNA and protein levels in ZIKV-infected brains. Furthermore, the rare polymorphisms we identified in PTPRZ1 raise the possibility of PTN-PTPRZ1 regulatory dysregulation and genetically driven suppression of neuroinflammation, which might result in a viral evasion mechanism. When considering the proteins that were exclusively detected in CZS brains and not in control brain (table S4), another gene found in all three omics layers was NRCAM. NRCAM is a cell adhesion molecule that can interact with PTPRZ1 (50).

We also observed rare mutations in genes related to the immune system, including C7, C8A, IL4R, IL7, IRF3, and TLR2. The variants found in C7 and C8A are present in the membrane attack complex/perforin (MACPF) domain. The activation of the alternative complement pathway begins with assembly of the MAC (cell-killing membrane attack complex) through the interaction of C5b with C6, C7, C8, and multiple C9 molecules. In flavivirus infections, the complement system may cause an exacerbated inflammatory response when excessively activated, increasing disease severity (51, 52). We found a variant in the Toll–interleukin-1 (IL-1) receptor homologous region (TIR) of Toll-like receptor 2 (TLR2), a receptor that plays a fundamental role in pathogen recognition and activation of innate immunity. This variant confers susceptibility to *Mycobacterium tuberculosis* infection and the incidence of other infectious diseases (53, 54). Upon activation, the TLR2 adaptor proteins Myd88 and TIRAP trigger signaling pathways that activate transcription factors, such as nuclear factor κB (NF-κB), interferon regulatory factor 3 (IRF3) and IRF7, and activating protein 1 (AP-1), which then translocate to the nucleus to induce the transcription of genes encoding interferons (IFNs) and proinflammatory cytokines. The autophagy process already demonstrated in ZIKV infection is a cellular catabolic pathway delivering cytoplasmic load to the lysosome for degradation and is considered as a primordial form of innate immunity against invading microorganisms (55). IRF3 plays a critical role in the innate immune response against DNA and RNA viruses, driving the transcription genes encoding type I IFNs (56). In addition, a mutation in the *IRF3* gene is associated with increased susceptibility to herpes simplex virus 1 (HSV-1) infection in the CNS in humans (57). SNPs in the gene encoding the IL-4 receptor (IL-4R) are also associated with increased susceptibility to dengue virus infection (58). These genetic variants that may affect the function of immune system genes may play a substantial role in the death of the neonates in our study by conferring susceptibility to the virus, enabling viral replication, or causing an increased inflammatory response to ZIKV infection, which may lead to CZS.

Together, our data from the examination of postmortem brain samples reveal the molecular basis of ZIKV infection after vertical transmission. Despite the small sample size, these brain samples are a valuable resource considering the decrease in CZS cases worldwide. Our systems biology approach enabled us to unveil the different layers of biological information associated with CZS.

MATERIALS AND METHODS
Patients and neuroimaging studies
From June 2015 to July 2016, pregnant women presenting at a clinic with acute febrile illness with a rash, fetal CNS abnormalities at prenatal ultrasonography, or postnatal microcephaly or other CNS malformation that was believed to be characteristic of congenital infection were referred to the Microcephaly Reference Center Instituto de Pesquisa Professor Amorim Neto (IPESQ) in Campina Grande (Paraíba, Brazil) or Instituto Fernandes Figueira–Fiocruz (Rio de Janeiro, Brazil). This study includes imaging and autopsy data from an institutional review board–approved study (52888616.4.0000.5693 and 52675616.0.000.5269) that allowed for imaging and follow-up of presumed ZIKV infection in pregnant women and their neonates. Written informed consent was obtained from the pregnant women, the parents of the neonates, or both. Detailed demographic, medical, and prenatal history information, as well as clinical findings, was entered into case report forms by multidisciplinary medical teams. All of the women were referred for at least one fetal ultrasonography during gestation. The onset symptoms included fever, exanthema, arthralgia, conjunctivitis, and headache in the pregnant women during gestation. The CNS of eight neonates who died in the first 48 hours of life (two of them immediately after delivery), three from northeastern (Campina Grande, Paraíba state) and five from southeastern Brazil (Rio de Janeiro) whose mothers reported typical symptoms of ZIKV infection until the 18th gestational week, were examined postmortem. Intrauterine fetal development was followed by ultrasonography and fetal MRI. Just after birth, the cephalic perimeter was measured, and the percentile was calculated according to that expected for gestational age 1. Prenatal ultrasonography was performed by fetal medicine specialists using either a Voluson E8 unit (General Electric) with transvaginal probes or a Samsung XG or WS80 unit (Samsung) with 2- to 9-MHz probes. MRI of the fetus was performed with a 3-T Skyra unit (Siemens Healthcare) or a 1.5-T Espree unit (Siemens Healthcare) with an eight-channel body coil and standard acquisition protocols. Postnatal head computed tomography (CT) was performed with a 16-section CT scanner (Siemens Healthcare). Postnatal MRI was performed with a 1.5-T Espree brain MRI unit (Siemens Healthcare). Brain tissue images were acquired with a 64-channel multisection CT scanner (GE Healthcare) and a 3-T MRI unit (Achieva).

Autopsies

Full autopsies were performed, and the brains were fixed in 10% buffered formalin. In the three cases from IPESQ, one hemisphere of the brain was stored in RNAlater (Thermo Fisher Scientific) and then frozen for viral RNA detection and both transcriptome and proteomic analyses. In seven cases, the whole spinal cords were also removed, four of them with dorsal root ganglia (DRG). The upper cervical spinal cord was also sampled in two other cases, one with DRG. Formalin-fixed brains were weighed, and the percentile was calculated according to the weights expected for the appropriate gestational age (59). In addition, samples from skeletal muscle (paravertebral, psoas, diaphragm, or adjacent to the head of the femur) were taken and examined histologically in five cases. After macroscopic examination, representative areas, including those with macroscopic lesions, were processed for paraffin embedding, and 5-μm histological sections were stained with hematoxylin and eosin. The neuropathological findings of these patients have been reported previously (10). Brains of ZIKV, CHIKV (chikungunya virus), DENV (dengue virus), or STORCH negative controls of the same gestational age (30th to 41st weeks of gestation) were obtained from Maternidade Escola, Universidade Federal do Rio de Janeiro (UFRJ; Rio de Janeiro, Brazil) in accordance with an institutional review board–approved study (1705093) and from Paraíba state. The cause of death of the negative control cases was genetic (trisomy of chromosome 18), acute perinatal anoxia, or complications of prematurity.

ZIKV diagnostic procedures

ZIKV RNA was investigated in the mothers or babies by RT-PCR analysis targeting the *env* gene as described by Lanciotti *et al.* (60). ZIKV RNA was detected in fluid samples, including blood, urine, amniotic fluid obtained by amniocentesis during gestation, or in other fluids after birth (amniotic fluid, cord blood, or both). The ZIKV genome was also investigated postnatally in the autopsied tissues (placenta, brain, and other organs). Viral RNA was extracted from 140 μl of fluid with QIAmp MiniElute Virus Spin (QIAgen) according to the manufacturer's recommendations. ZIKV RNA detection was performed by One-Step TaqMan RT-PCR (Thermo Fisher Scientific) on a 7500 Real-Time PCR System (Applied Biosystems) with primers, probes, and conditions as described previously (4). Fifty milligrams of frozen organs, such as cerebral cortex, heart, skin, spleen, thymus, liver, kidneys, lung, and placenta, was disrupted with a TissueRuptor (QIAgen) with 325 μl of RTL buffer from the RNeasy Plus Mini Kit (QIAgen) according to the manufacturer's protocol. RNA extraction was performed with the RNeasy Plus Mini Kit (QIAgen) according to the manufacturer's instructions. Real-time RT-PCR was performed with 1 μg of total tissue RNA using One-Step TaqMan RT-PCR (Thermo Fisher Scientific) as described earlier. Dengue and chikungunya virus infections were excluded in all cases (fluids and tissues) either by RT-PCR analysis with ZDC Trioplex kits (Bio-Manguinhos) or serological enzyme-linked immunosorbent assay (ELISA) for the detection of immunoglobulin M (IgM) and IgG (Kit xGen, Biometrix, and Euroimmum kit). Other congenital pathogens, including syphilis, cytomegalovirus, herpes virus 1/2, *Toxoplasma gondii*, and rubella virus (STORCH), were investigated by serological ELISA against IgM (Dia.Pro Diagnostic Bioprobes) according to the manufacturer's recommendations. ZIKV RNA ISH was performed on formalin-fixed, paraffin-embedded tissue sections of all brain tissues with two commercial RNAscope target probes (Advanced Cell Diagnostics; catalog numbers 464531 and 463781

complementary to sequences 866–1763 and 1550–2456 of the ZIKV genome, respectively). Pretreatment, hybridization, and detection techniques were performed according to the manufacturer's protocols as previously described (10).

Collagen staining/immunohistochemistry

For total collagen visualization, paraffin-embedded sections from formalin-fixed fragments of postmortem brains were stained with Gomori's trichrome reagent. Immunohistochemical analysis of the leptomeninges and the choroid plexus of ZIKV cases and controls was performed with anti–collagen type 1 (Sigma-Aldrich, clone col-1) at a dilution of 1:1000. Briefly, 5-μm-thick tissue sections were incubated in an oven at 37°C for 6 hours, deparaffinized in xylene, rehydrated by being placed in decreasing concentrations of alcohol, and washed in distilled water. To enhance antigen retrieval, the tissue sections were pretreated in a pressure cooker for 15 min in a solution of 1/20 Declare (pH 6)/1/100 Trilogy (pH 9) in distilled water. To block endogenous peroxidase activity, the samples were exposed to hydrogen peroxide, washed with distilled water, and rinsed in phosphate-buffered saline (PBS) to stop enzymatic digestion. The samples were then incubated with the primary antibody overnight at 4°C, rinsed in PBS for 5 min, and incubated with Polymer Hi-Def (horseradish peroxidase system) for 10 min at room temperature followed by several washes in PBS. The peroxidase reaction was visualized by incubating the sections with 3,3′-diaminobenzidine (DAB) substrate and then rinsing in running water. The sections were then counterstained with Mayer's hematoxylin for 1 min, washed in running tap water for 3 min, dehydrated in alcohol, cleared in xylene, and mounted in a resinous medium. Quantification of collagen abundance as assessed by histopathological analysis was performed with ImageJ software (61). For images from Gomori's trichrome staining, the extension plugin Color Deconvolution was used as described previously (62). For DAB immunohistochemical staining, quantification was performed with the Immunohistochemistry Profiler plugin (63). Results were expressed on integrated density (area × intensity) of collagen staining. Statistical analysis (unpaired *t* tests) was performed with Prism8 software.

Library preparation and RNA-seq

Brain samples were frozen in RNAlater (Ambion) and stored at −80°C until extraction. The tissue was broken and homogenized with TissueRuptor (QIAgen), and RNA extraction was performed with the RNeasy Plus Mini Kit (QIAgen) according to the manufacturer's protocol. The integrity of RNA was evaluated with an Agilent 2100 Bioanalyzer and RNA 6000 Pico. Total RNA was quantified by the Quant-iT RiboGreen RNA Reagent and Kit (Invitrogen, Life Technologies Corp.), and the complementary DNA (cDNA) library was constructed according to the SMARTer Stranded Total RNA-Seq Peak Input Mammalian Kit protocol (Takara Bio USA). The size distribution of the cDNA library was measured by the 2100 Bioanalyzer and quantitated before sequencing with the Quant-iT PicoGreen RNA Reagent and Kit (Invitrogen, Life Technologies Corp.). The libraries were diluted to 4 nM with 15% PhiX. The cDNA library was sequenced with MiSeq System (Illumina) using the MiSeq Reagent Kit (150 cycles, 2 × 75 paired-end).

Preprocessing and analysis of RNA-seq data

FASTQ quality control was performed with the FastQC tool (www.bioinformatics.babraham.ac.uk/projects/fastqc/). Paired-end reads

were aligned to the human genome, ENSEMBL GRCh38.89, by STAR v.2.5.3.a, an ultrafast aligner (*64*). The aligned reads were then quantified with featureCounts v.1.5.3 (*65*). DEGs between control and infected conditions were detected with DESeq2 v.1.16.1 R package (*66*) (adjusted *P* < 0.1). Functional enrichment analysis was performed with Reactome pathways (https://reactome.org/) and the Enrichr tool (*67*) for overrepresentation analysis. The overlap between gene lists was analyzed with the circlize (*68*) and UpSetR (*69*) packages. The transcriptomic dataset associated with our work is publicly available at GEO (www.ncbi.nlm.nih.gov/geo/) with the project accession number GSE125554.

DNA extraction for whole-exome sequencing

Genomic DNA was extracted from the CNS. Exome sequencing libraries were prepared with the Illumina TruSeq Exome Kit (8 rxn × 6plex). Sequencing was performed with an Illumina NextSeq 500/550 High Output Kit v2 (150 cycles), generating 2 × 75 base pair paired-end reads.

Whole-exome sequencing analysis

The quality of the exome libraries was evaluated with the FastQC tool (www.bioinformatics.babraham.ac.uk/projects/fastqc/). The removal of reads or fragments with low quality was performed with Trimmomatic software (www.usadellab.org/cms/?page=trimmomatic). The resulting high-quality reads were aligned with the human genome as a reference (version GRCh38) using Bowtie2 (*70*) with the very sensitive default preset (-D 20 -R 3 -N 1 -L 20 -i S,1,0.50), except to one mismatch per seed region (-N 1). The optical duplicates were marked with the mark duplicates tool (http://broadinstitute.github.io/picard/). Furthermore, the Genome Analysis Toolkit (GATK) version 3.7 (*71*) was used to call single-nucleotide variants, small insertions and deletions (INDELs). All variants were annotated with the HaplotypeCaller according to the GATK best practices manual (*72, 73*). The variant calls with a read coverage of ≤5 reads or a MAP quality of ≤30 were filtered out to avoid false positives. The SnpEff (*74*) and SnpSift (*75*) version 4.3r tools were used to predict and annotate the functional effect of variants with the dbSNP (build 151) (*76*) and dbNSFP (version 3.5) (*77*) databases. The variants with an MAF ≤5% in at least one of the following databases (retrieved from dbNSFP database version 3.5) were considered: 1000 Genomes Project Phase 3 (http://internationalgenome.org/), gnomAD (http://gnomad.broadinstitute.org/), TOPMed (https://nhlbiwgs.org/), ESP6500 (http://evs.gs.washington.edu/EVS/), TwinsUK (http://twinsuk.ac.uk/), Avon Longitudinal Study of Parents and Children (ALSPAC) (http://bris.ac.uk/alspac/), and ABraOM (http://abraom.ib.usp.br/). We also verified the presence of variants in the GWAS (Genome-wide association studies) catalog (retrieved from www.ebi.ac.uk/gwas/) and ClinVar, release 20180603 (https://ncbi.nlm.nih.gov/clinvar/). The 1000 Genomes Project Phase 3, ExAC, and gnomAD included African, admixed American, East Asian, European, South Asian, and non-Finnish European populations. The TOPMed and ESP6500 included cohorts from the United States. The TwinsUK included old-aged twins from the United Kingdom, and ALSPAC included European cohorts. ABraOM is a variant repository comprising a cohort of elderly Brazilians (*78*). We considered only those variants with a Combined Annotation Dependent Depletion (CADD) score ≥15 (*79*) and used a set of functional effect predictors, such as MetaSVM, FATHMM, LRT, PROVEAN, Polyphen2-HDIV, Polyphen2-HVAR, MutationTaster, Mutation Assessor, and SIFT for variant prioritization (*80*). All variants

of interest were manually inspected with the IGV (Integrative Genomics Viewer) tool (*81*). We consulted protein domain databases, such as Panther (http://pantherdb.org), Pfam (https://pfam.xfam.org), Interpro (www.ebi.ac.uk/interpro), SMART (http://smart.embl-heidelberg.de/), and PROSITE (https://prosite.expasy.org/) to evaluate the domains that could be affected by genetic variants. The exome dataset associated with our work is publicly available in Sequence Read Archive (SRA)–National Center for Biotechnology Information (NCBI) (www.ncbi.nlm.nih.gov/sra) with SRA accession number PRJNA517145.

Protein extraction

About 30 mg of brain tissue was homogenized with 1.5 ml of extraction solution containing 5% sodium deoxycholate (SDC), 0.75 mM dithiothreitol (DTT), and protease and phosphatase inhibitors (Roche) in a TissueRuptor (QIAgen). After incubation for 20 min at 80°C, the solution was vortexed for 20 s and centrifuged at 20,000g for 30 min at 4°C. The pellet from overnight precipitation of 400 μl of the supernatant with cold acetone (ratio 1:4) was washed twice with acetone, centrifuged at 20,000g for 15 min at 4°C, and then dried. After solubilizing with 7 M urea, 2 M thiourea with 2% SDC, we used the Qubit protein assay Kit (Invitrogen) to measure protein content according to the manufacturer's instructions.

Enzymatic digestion

Reduction and alkylation of 100 μg of soluble proteins required 10 mM DTT for 1 hour at 30°C and 40 mM iodoacetamide (IAA) for 30 min at room temperature in the dark. Samples were diluted 1:10 with 100 mM triethylammonium bicarbonate buffer (pH 8.5) and digested with trypsin (1:25, w/w) for 18 hours at 35°C. The addition of a final concentration of 1% trifluoroacetic acid (TFA) stopped the digestion, and two centrifugations at 20,000g for 15 min at 4°C removed the SDC. Last, samples were desalted in Macro SpinColumns C_{18} (Harvard Apparatus) and dried in a vacuum concentrator (Martin Christ). Peptides were suspended in 15 μl of 0.1% formic acid and quantified with the Qubit protein assay as described by the manufacturer.

Nano-LC MS² analysis

Each sample was analyzed four times (four technical replicates) in an EASY-nLC 1000 (Thermo Scientific) coupled to a Q-Exactive Plus mass spectrometer (Thermo Scientific). The peptide mixture (2 μg) was loaded in a homemade, 3-cm trap column, 200-μm internal diameter (ID), 5-μm Reprosil-Pur C18-AQ (Dr. Maisch) beads and fractionated in a 20-cm Self-Pack PicoFrit analytical column (New Objective), 75-μm ID, 3-μm Reprosil-Pur C18-AQ (Dr. Maisch). The nano–liquid chromatography (nLC) gradient fractionation lasted for 180 min and had a flow rate of 250 nl/min: 167 min, from 5 to 40% solvent B (95% ACN/5% H_2O/0.1% formic acid); 5 min, from 40 to 95% solvent B; and 8 min in 95% solvent B. The column and trap were equilibrated with solvent A [95% H_2O/5% acetonitrile (ACN)/0.1% formic acid] after each run for 15 and 2 min, respectively. The instrument was set in the positive polarity and full-MS/dd-MS² mode. Selected full-scan parameters were as follows: 1 microscan, 70,000 resolution at 200 mass/charge ratio (m/z), 3 × 10⁶ ions for the AGC target, 50-ms maximum injection time, and a range of 375 to 2000 m/z. The top 20 dd-MS² parameters were as follows: 17,000 resolution, 200 m/z, 1 × 10⁵ ions for the AGC target, maximum injection time of 100 ms, 1.2 Th of isolation window, Normalized Collision Energy (NCE) of 30, minimum intensity threshold of 10,000 ions, and dynamic exclusion of 60 s.

Proteomics analysis

For database searches, raw data were processed with Proteome Discoverer 2.1 (PD2.1) software (Thermo Scientific) and the SuperQuant strategy performed by nodes MSn Deconvolution and Complementary Finder as described previously (82). Searches performed against all reviewed human and virus entries present in the UniProt database (Jan/2017) used the Sequest HT algorithm. Viral proteins were not considered for the analyses. The parameters used for the search were as follows: full tryptic peptides, two missed cleavages allowed, precursor mass tolerance of 10 parts per million, 0.1 Da product ion mass tolerance, cysteine carbamidomethylation as fixed modification, and methionine oxidation and protein N-terminal acetylation as variable modifications. To estimate the false discovery rate (FDR) of <1%, we used the node Percolator present in the PD2.1 using maximum parsimony. A cutoff score was established to accept an FDR of 1% at the protein and peptide levels, and proteins were grouped in master proteins using the maximum parsimony principle. Quantification used the workflow node Precursor Ions Area Detector in PD2.1. The peak areas estimated by the extracted ion chromatogram (XIC) for the three most abundant distinct peptides of each protein were averaged and used for relative quantification. Statistical analysis was performed with Perseus version 1.6.0.7. (83). Data were converted to a $\log_2$ scale and normalized by subtracting the converted protein area value (XIC) from the median of the sample distribution. Only proteins with peak area averages present in at least three runs were used for quantitative evaluation. We used the limma R package (84) to identify the proteins that were increased or decreased in abundance in CZS brains compared with those in the control brain. A cutoff adjusted P value of <0.1 was used. Proteins detected in at least two CZS samples and not detected in the control were considered to be exclusively expressed in CZS samples. Proteins detected in the control and not detected in any of the CZS samples were considered to be exclusively expressed in the control. Functional enrichment analysis was performed with Reactome pathways (https://reactome.org/) and the Enrichr tool (67) for overrepresentation analysis. The proteomics dataset associated with this study is publicly available in ProteomeXchange (www.proteomexchange.org/) with project accession number PXD012461.

Network analysis

PPI networks and the miRNA-gene network were generated with the NetworkAnalyst tool (85). PPIs (edges) were retrieved from the STRING interactome with a confidence score of 900. The miRNA-gene interaction data were collected from TarBase and miRTarBase (validated interactions). We used the Minimum Network tool to include the seed genes/proteins [that is, the DEGs or DEPs (differentially expressed proteins)], as well as the essential nonseed genes/proteins that kept the network connection. Cytoscape (86) was also used to visualize the networks.

SUPPLEMENTARY MATERIALS

stke.sciencemag.org/cgi/content/full/13/635/eaay6736/DC1

Fig. S1. Modulation of brain-expressed genes in neonates with CZS as evidenced by transcriptomic analysis.

Fig. S2. Comparison with publicly available transcriptomic signatures of human cells infected in vitro with ZIKV.

Fig. S3. A network of highly associated CZS-related genes.

Table S1. Clinical and brain autopsy findings of CZS cases.

Table S2. Brain histopathological observations.

Table S3. Transcriptomic analysis results.

Table S4. Proteomic analysis results.

Table S5. Genomic analysis results.

View/request a protocol for this paper from *Bio-protocol*.

REFERENCES AND NOTES

1. A. Suely de Oliveira Melo, R. S. Aguiar, M. M. R. Amorim, M. B. Arruda, F. de Oliveira Melo, S. T. C. Ribeiro, A. G. M. Batista, T. Ferreira, M. P. Dos Santos, V. V. Sampaio, S. R. M. Moura, L. P. Rabello, C. E. Gonzaga, G. Malinger, R. Ximenes, P. Soares, de Oliveira-Szejnfeld, F. Tovar-Moll, L. Chimelli, P. P. Silveira, R. Delvechio, L. Higa, L. Campanati, R. M. R. Nogueira, A. M. B. Filippis, J. Szejnfeld, C. M. Voloch, O. C. Ferreira Jr., R. M. Brindeiro, A. Tanuri, Congenital Zika virus infection: Beyond neonatal microcephaly. *JAMA Neurol.* **73**, 1407–1416 (2016).

2. J. Mlakar, M. Korva, N. Tul, M. Popović, M. Poljšak-Prijatelj, J. Mraz, M. Kolenc, K. R. Rus, T. V. Vipotnik, V. F. Vodušek, A. Vizjak, J. Pižem, M. Petrovec, T. A. Županc, Zika virus associated with microcephaly. *N. Engl. J. Med.* **374**, 951–958 (2016).

3. C. V. Ventura, M. Maia, V. Bravo-Filho, A. L. Góis, R. Belfort Jr., Zika virus in Brazil and macular atrophy in a child with microcephaly. *Lancet* **387**, 228 (2016).

4. P. Brasil, J. P. Pereira Jr., M. E. Moreira, R. M. R. Nogueira, L. Damasceno, M. Wakimoto, R. S. Rabello, S. G. Valderramos, U.-A. Halai, T. S. Salles, A. A. Zin, D. Horovitz, P. Daltro, M. Boechat, C. R. Gabaglia, P. C. de Sequeira, J. H. Pilotto, R. Medialdea-Carrera, D. C. da Cunha, L. M. A. de Carvalho, M. Pone, A. M. Siqueira, G. A. Calvet, A. E. R. Baião, E. S. Neves, P. R. N. de Carvalho, R. H. Hasue, P. B. Marschik, C. Einspieler, C. Janzen, J. D. Cherry, A. M. B. de Filippis, K. Nielsen-Saines, Zika virus infection in pregnant women in Rio de Janeiro. *N. Engl. J. Med.* **375**, 2321–2334 (2016).

5. M. R. Duffy, T.-H. Chen, W. T. Hancock, A. M. Powers, J. L. Kool, R. S. Lanciotti, M. Pretrick, M. Marfel, S. Holzbauer, C. Dubray, L. Guillaumot, A. Griggs, M. Bel, A. J. Lambert, J. Laven, O. Kosoy, A. Panella, B. J. Biggerstaff, M. Fischer, E. B. Hayes, Zika virus outbreak on Yap Island, Federated States of Micronesia. *N. Engl. J. Med.* **360**, 2536–2543 (2009).

6. M. A. Johansson, L. Mier-y-Teran-Romero, J. Reefhuis, S. M. Gilboa, S. L. Hills, Zika and the risk of microcephaly. *N. Engl. J. Med.* **375**, 1–4 (2016).

7. C. A. Moore, J. E. Staples, W. B. Dobyns, A. Pessoa, C. V. Ventura, E. B. da Fonseca, E. M. Ribeiro, L. O. Ventura, N. N. Neto, J. F. Arena, S. A. Rasmussen, Characterizing the pattern of anomalies in congenital Zika syndrome for pediatric clinicians. *JAMA Pediatr.* **171**, 288–295 (2017).

8. H. Tang, C. Hammack, S. C. Ogden, Z. Wen, X. Qian, Y. Li, B. Yao, J. Shin, F. Zhang, E. M. Lee, K. M. Christian, R. A. Didier, P. Jin, H. Song, G.-l. Ming, Zika virus infects human cortical neural progenitors and attenuates their growth. *Cell Stem Cell* **18**, 587–590 (2016).

9. Q. Shao, S. Herrlinger, S.-L. Yang, F. Lai, J. M. Moore, M. A. Brindley, J.-F. Chen, Zika virus infection disrupts neurovascular development and results in postnatal microcephaly with brain damage. *Development* **143**, 4127–4136 (2016).

10. L. Chimelli, A. S. O. Melo, E. Avvad-Portari, C. A. Wiley, A. H. S. Camacho, V. S. Lopes, H. N. Machado, C. V. Andrade, D. C. A. Dock, M. E. Moreira, F. Tovar-Moll, P. S. Oliveira-Szejnfeld, A. C. G. Carvalho, O. N. Ugarte, A. G. M. Batista, M. M. R. Amorim, F. O. Melo, T. A. Ferreira, J. R. L. Marinho, G. S. Azevedo, J. I. B. F. Leal, R. F. Madeiro da Costa, S. Rehen, M. B. Arruda, R. M. Brindeiro, R. Delvechio, R. S. Aguiar, A. Tanuri, The spectrum of neuropathological changes associated with congenital Zika virus infection. *Acta Neuropathol.* **133**, 983–999 (2017).

11. P. P. Garcez, J. M. Nascimento, J. M. de Vasconcelos, R. M. da Costa, R. Delvecchio, P. Trindade, E. C. Loiola, L. M. Higa, J. S. Cassoli, G. Vitória, P. C. Sequeira, J. Sochacki, R. S. Aguiar, H. T. Fuzii, A. M. B. de Filippis, J. L. da Silva Gonçalves Vianez Júnior, A. Tanuri, D. Martins-de-Souza, S. K. Rehen, Zika virus disrupts molecular fingerprinting of human neurospheres. *Sci. Rep.* **7**, 40780 (2016).

12. M. Kwissa, H. I. Nakaya, N. Onlamoon, J. Wrammert, F. Villinger, G. C. Perng, S. Yoksan, K. Pattanapanyasat, K. Chokephaibulkit, R. Ahmed, B. Pulendran, Dengue virus infection induces expansion of a CD14$^+$CD16$^+$ monocyte population that stimulates plasmablast differentiation. *Cell Host Microbe* **16**, 115–127 (2014).

13. H. I. Nakaya, B. Pulendran, Vaccinology in the era of high-throughput biology. *Philos. Trans. R. Soc. Lond. B Biol. Sci.* **370**, 20140146 (2015).

14. HIPC-CHI Signatures Project Team; HIPC-I Consortium, Multicohort analysis reveals baseline transcriptional predictors of influenza vaccination responses. *Sci. Immunol.* **2**, eaal4656 (2017).

15. B. Hoen, B. Schaub, A. L. Funk, V. Ardillon, M. Boullard, A. Cabié, C. Callier, G. Carles, S. Cassadou, R. Césaire, M. Douine, C. Herrmann-Storck, P. Kadhel, C. Laouénan, Y. Madec, A. Monthieux, M. Nacher, F. Najioullah, D. Rousset, C. Ryan, K. Schepers, S. Stegmann-Planchard, B. Tressières, J.-L. Voluménie, S. Yassinguezo, E. Janky, A. Fontanet, Pregnancy outcomes after ZIKV infection in French territories in the Americas. *N. Engl. J. Med.* **378**, 985–994 (2018).

16. E. R. Krow-Lucal, M. R. de Andrade, J. N. A. Cananéa, C. A. Moore, P. L. Leite, B. J. Biggerstaff, C. M. Cabral, M. Itoh, J. Percio, M. Y. Wada, A. M. Powers, A. Barbosa, R. B. Abath, J. E. Staples, G. E. Coelho; Paraíba Microcephaly Work Group, Association

and birth prevalence of microcephaly attributable to Zika virus infection among infants in Paraiba, Brazil, in 2015-16: A case-control study. *Lancet Child Adolesc.* **2**, 205–213 (2018).

17. V. V. Costa, J. L. Del Sarto, R. F. Rocha, F. R. Silva, J. G. Doria, I. G. Olmo, R. E. Marques, C. M. Queiroz-Junior, G. Foureaux, J. M. S. Araújo, A. Cramer, A. L. C. V. Real, L. S. Ribeiro, S. I. Sardi, A. J. Ferreira, F. S. Machado, A. C. de Oliveira, A. L. Teixeira, H. I. Nakaya, D. G. Souza, F. M. Ribeiro, M. M. Teixeira, *N*-methyl-D-aspartate (NMDA) receptor blockade prevents neuronal death induced by Zika virus infection. *MBio* **8**, e00350-17 (2017).

18. B. Obermeier, R. Daneman, R. M. Ransohoff, Development, maintenance and disruption of the blood-brain barrier. *Nat. Med.* **19**, 1584–1596 (2013).

19. J. G. S. Mala, C. Rose, Interactions of heat shock protein 47 with collagen and the stress response: An unconventional chaperone model? *Life Sci.* **87**, 579–586 (2010).

20. S. Deckx, S. Heymans, A.-P. Papageorgiou, The diverse functions of osteoglycin: A deceitful dwarf, or a master regulator of disease? *FASEB J.* **30**, 2651–2661 (2016).

21. R. A. Kozak, A. Majer, M. J. Biondi, S. J. Medina, L. W. Goneau, B. V. Sajesh, J. A. Slota, V. Zubach, A. Severini, D. Safronetz, S. L. Hiebert, D. R. Beniac, T. F. Booth, S. A. Booth, G. P. Kobinger, MicroRNA and mRNA dysregulation in astrocytes infected with Zika virus. *Viruses* **9**, 297 (2017).

22. K. Kuboyama, A. Fujikawa, M. Masumura, R. Suzuki, M. Matsumoto, M. Noda, Protein tyrosine phosphatase receptor type Z negatively regulates oligodendrocyte differentiation and myelination. *PLOS ONE* **7**, e48797 (2012).

23. J. D. Buxbaum, L. Georgieva, J. J. Young, C. Plescia, Y. Kajiwara, Y. Jiang, V. Moskvina, N. Norton, T. Peirce, H. Williams, N. J. Craddock, L. Carroll, G. Corfas, K. L. Davis, M. J. Owen, S. Harroch, T. Sakurai, M. C. O'Donovan, Molecular dissection of NRG1-ERBB4 signaling implicates PTPRZ1 as a potential schizophrenia susceptibility gene. *Mol. Psychiatr.* **13**, 162–172 (2008).

24. K. S. Christopherson, E. M. Ullian, C. C. A. Stokes, C. E. Mullowney, J. W. Hell, A. Agah, J. Lawler, D. F. Mosher, P. Bornstein, B. A. Barres, Thrombospondins are astrocyte-secreted proteins that promote CNS synaptogenesis. *Cell* **120**, 421–433 (2005).

25. K. A. Robinson, M. Sun, C. E. Barnum, S. N. Weiss, J. Huegel, S. S. Shetye, L. Lin, D. Saez, S. M. Adams, R. V. Iozzo, L. J. Soslowsky, D. E. Birk, Decorin and biglycan are necessary for maintaining collagen fibril structure, fiber realignment, and mechanical properties of mature tendons. *Matrix Biol.* **64**, 81–93 (2017).

26. A. M. Wojtas, S. S. Kang, B. M. Olley, M. Gatherer, M. Shinohara, P. A. Lozano, C.-C. Liu, A. Kurti, K. E. Baker, D. W. Dickson, M. Yue, L. Petrucelli, G. Bu, R. O. Carare, J. D. Fryer, Loss of clusterin shifts amyloid deposition to the cerebrovasculature via disruption of perivascular drainage pathways. *Proc. Natl. Acad. Sci. U.S.A.* **114**, E6962–E6971 (2017).

27. K. M. Baeten, K. Akassoglou, Extracellular matrix and matrix receptors in blood-brain barrier formation and stroke. *Dev. Neurobiol.* **71**, 1018–1039 (2011).

28. R. Hamel, O. Dejarnac, S. Wichit, P. Ekchariyawat, A. Neyret, N. Luplertlop, M. Perera-Lecoin, P. Surasombatpattana, L. Talignani, F. Thomas, V.-M. Cao-Lormeau, V. Choumet, L. Briant, P. Desprès, A. Amara, H. Yssel, D. Missé, Biology of Zika virus infection in human skin cells. *J. Virol.* **89**, 8880–8896 (2015).

29. M. Aid, P. Abbink, R. A. Larocca, M. Boyd, R. Nityanandam, O. Nanayakkara, A. J. Martinot, E. T. Moseley, E. Blass, E. N. Borducchi, A. Chandrashekar, A. L. Brinkman, K. Molloy, D. Jetton, L. J. Tartaglia, J. Liu, K. Best, A. S. Perelson, R. A. De La Barrera, M. G. Lewis, D. H. Barouch, Zika virus persistence in the central nervous system and lymph nodes of rhesus monkeys. *Cell* **169**, 610–620.e14 (2017).

30. D. S. Kuo, C. Labelle-Dumais, D. B. Gould, COL4A1 and COL4A2 mutations and disease: Insights into pathogenic mechanisms and potential therapeutic targets. *Hum. Mol. Genet.* **21**, R97–R110 (2012).

31. E. Pöschl, U. Schlötzer-Schrehardt, B. Brachvogel, K. Saito, Y. Ninomiya, U. Mayer, Collagen IV is essential for basement membrane stability but dispensable for initiation of its assembly during early development. *Development* **131**, 1619–1628 (2004).

32. R. Dittrich, A. Heidbreder, D. Rohsbach, J. Schmalhorst, I. Nassenstein, D. Maintz, E. B. Ringelstein, D. G. Nabavi, G. Kuhlenbäumer, Connective tissue and vascular phenotype in patients with cervical artery dissection. *Neurology* **68**, 2120–2124 (2007).

33. Y.-C. Weng, A. Sonni, C. Labelle-Dumais, M. de Leau, W. B. Kauffman, M. Jeanne, A. Biffi, S. M. Greenberg, J. Rosand, D. B. Gould, COL4A1 mutations in patients with sporadic late-onset intracerebral hemorrhage. *Ann. Neurol.* **71**, 470–477 (2012).

34. E. Faqeih, P. Roughley, F. H. Glorieux, F. Rauch, Osteogenesis imperfecta type III with intracranial hemorrhage and brachydactyly associated with mutations in exon 49 of COL1A2. *Am. J. Med. Genet. A* **149A**, 461–465 (2009).

35. Z. Zhu, M. J. Gorman, L. D. McKenzie, J. N. Chai, C. G. Hubert, B. C. Prager, E. Fernandez, J. M. Richner, R. Zhang, C. Shan, E. Tycksen, X. Wang, P.-Y. Shi, M. S. Diamond, J. N. Rich, M. G. Chheda, Zika virus has oncolytic activity against glioblastoma stem cells. *J. Exp. Med.* **214**, 3145 (2017).

36. Q. Chen, J. Wu, Q. Ye, F. Ma, Q. Zhu, Y. Wu, C. Shan, X. Xie, D. Li, X. Zhan, C. Li, X.-F. Li, X. Qin, T. Zhao, H. Wu, P.-Y. Shi, J. Man, C.-F. Qin, Treatment of human glioblastoma with a live attenuated Zika virus vaccine candidate. *MBio* **9**, e01683-18 (2018).

37. T. Mammoto, A. Jiang, E. Jiang, D. Panigrahy, M. W. Kieran, A. Mammoto, Role of collagen matrix in tumor angiogenesis and glioblastoma multiforme progression. *Am. J. Pathol.* **183**, 1293–1305 (2013).

38. P. Ferraris, M. Cochet, R. Hamel, I. Gladwyn-Ng, C. Alfano, F. Diop, D. Garcia, L. Talignani, C. N. Montero-Menei, A. Nougairède, H. Yssel, L. Nguyen, M. Coulpier, D. Missé, Zika virus differentially infects human neural progenitor cells according to their state of differentiation and dysregulates neurogenesis through the Notch pathway. *Emerg. Microbes Infec.* **8**, 1003–1016 (2019).

39. J. F. Bateman, R. P. Boot-Handford, S. R. Lamandé, Genetic diseases of connective tissues: Cellular and extracellular effects of ECM mutations. *Nat. Rev. Genet.* **10**, 173–183 (2009).

40. J. C. Marini, A. Forlino, W. A. Cabral, A. M. Barnes, J. D. San Antonio, S. Milgrom, J. C. Hyland, J. Körkkö, D. J. Prockop, A. De Paepe, P. Coucke, S. Symoens, F. H. Glorieux, P. J. Roughley, A. M. Lund, K. Kuurila-Svahn, H. Hartikka, D. H. Cohn, D. Krakow, M. Mottes, U. Schwarze, D. Chen, K. Yang, C. Kuslich, J. Troendle, R. Dalgleish, P. H. Byers, Consortium for osteogenesis imperfecta mutations in the helical domain of type I collagen: Regions rich in lethal mutations align with collagen binding sites for integrins and proteoglycans. *Hum. Mutat.* **28**, 209–221 (2007).

41. H. Plotkin, Syndromes with congenital brittle bones. *BMC Pediatr.* **4**, 16 (2004).

42. Y. Zou, D. Zwolanek, Y. Izu, S. Gandhy, G. Schreiber, K. Brockmann, M. Devoto, Z. Tian, Y. Hu, G. Veit, M. Meier, J. Stetefeld, D. Hicks, V. Straub, N. C. Voermans, D. E. Birk, E. R. Barton, M. Koch, C. G. Bönnemann, Recessive and dominant mutations in COL12A1 cause a novel EDS/myopathy overlap syndrome in humans and mice. *Hum. Mol. Genet.* **23**, 2339–2352 (2014).

43. W. L. Siqueira, E. B. Moffa, M. C. M. Mussi, M. A. d. A. M. Machado, Zika virus infection spread through saliva — A truth or myth? *Braz. Oral Res.* **30**, S1806-83242016000100801 (2016).

44. B. Nadarajah, P. Alifragis, R. O. L. Wong, J. G. Parnavelas, Neuronal migration in the developing cerebral cortex: Observations based on real-time imaging. *Cereb. Cortex* **13**, 607–611 (2003).

45. P. F. Maness, M. Schachner, Neural recognition molecules of the immunoglobulin superfamily: Signaling transducers of axon guidance and neuronal migration. *Nat. Neurosci.* **10**, 263 (2007).

46. S. A. Teichmann, C. Chothia, Immunoglobulin superfamily proteins in *Caenorhabditis elegans. J. Mol. Biol.* **296**, 1367–1383 (2000).

47. F. R. Cugola, I. R. Fernandes, F. B. Russo, B. C. Freitas, J. L. M. Dias, K. P. Guimarães, C. Benazzato, N. Almeida, G. C. Pignatari, S. Romero, C. M. Polonio, I. Cunha, C. L. Freitas, W. N. Brandão, C. Rossato, D. G. Andrade, d. d. P. Faria, A. T. Garcez, C. A. Buchpigel, C. T. Braconi, E. Mendes, A. A. Sall, P. M. d. A. Zanotto, J. P. S. Peron, A. R. Muotri, P. C. B. Beltrão-Braga, The Brazilian Zika virus strain causes birth defects in experimental models. *Nature* **534**, 267–271 (2016).

48. R. Fernández-Calle, M. Vicente-Rodríguez, E. Gramage, J. Pita, C. Pérez-García, M. Ferrer-Alcón, M. Uribarri, M. P. Ramos, G. Herradón, Pleiotrophin regulates microglia-mediated neuroinflammation. *J. Neuroinflammation* **14**, 46 (2017).

49. H. Pariser, L. Ezquerra, G. Herradon, P. Perez-Pinera, T. F. Deuel, Fyn is a downstream target of the pleiotrophin/receptor protein tyrosine phosphatase beta/xi-signaling pathway: Regulation of tyrosine phosphorylation of Fyn by pleiotrophin. *Biochem. Biophys. Res. Commun.* **332**, 664–669 (2005).

50. T. Sakurai, M. Lustig, M. Nativ, J. J. Hemperly, J. Schlessinger, E. Peles, M. Grumet, Induction of neurite outgrowth through contactin and Nr-CAM by extracellular regions of glial receptor tyrosine phosphatase β. *J. Cell Biol.* **136**, 907–918 (1997).

51. J. N. Conde, E. M. Silva, A. S. Barbosa, R. Mohana-Borges, The complement system in flavivirus infections. *Front. Microbiol.* **8**, 213 (2017).

52. B. Schiela, S. Bernklau, Z. Malekshahi, D. Deutschmann, I. Koske, Z. Banki, N. M. Thielens, R. Würzner, C. Speth, G. Weiss, K. Stiasny, E. Steinmann, H. Stoiber, Active human complement reduces the Zika virus load via formation of the membrane-attack complex. *Front. Immunol.* **9**, 2177 (2018).

53. N. W. J. Schröder, I. Diterich, A. Zinke, J. Eckert, C. Draing, V. v. Baehr, D. Hassler, S. Priem, K. Hahn, K. S. Michelsen, T. Hartung, G. R. Burmester, U. B. Göbel, C. Hermann, R. R. Schumann, Heterozygous Arg753Gln polymorphism of human TLR-2 impairs immune activation by *Borrelia burgdorferi* and protects from late stage Lyme disease. *J. Immunol.* **175**, 2534–2540 (2005).

54. A. C. Ogus, B. Yoldas, T. Ozdemir, A. Uguz, S. Olcen, I. Keser, M. Coskun, A. Cilli, O. Yegin, The Arg753GLn polymorphism of the human toll-like receptor 2 gene in tuberculosis disease. *Eur. Respir. J.* **23**, 219–223 (2004).

55. R. Gratton, A. Agrelli, P. M. Tricarico, L. Brandão, S. Crovella, Autophagy in Zika virus infection: A possible therapeutic target to counteract viral replication. *Int. J. Mol. Sci.* **20**, 1048 (2019).

56. S. Liu, X. Cai, J. Wu, Q. Cong, X. Chen, T. Li, F. Du, J. Ren, Y.-T. Wu, N. V. Grishin, Z. J. Chen, Phosphorylation of innate immune adaptor proteins MAVS, STING, and TRIF induces IRF3 activation. *Science* **347**, aaa2630 (2015).

57. L. L. Andersen, N. Mørk, L. S. Reinert, E. Kofod-Olsen, R. Narita, S. E. Jørgensen, K. A. Skipper, K. Höning, H. H. Gad, L. Østergaard, T. F. Ørntoft, V. Hornung, S. R. Paludan,

J. G. Mikkelsen, T. Fujita, M. Christiansen, R. Hartmann, T. H. Mogensen, Functional IRF3 deficiency in a patient with herpes simplex encephalitis. *J. Exp. Med.* **212**, 1371–1379 (2015).

58. Y. M. Useche, B. N. Restrepo, D. M. Salgado, C. F. Narváez, O. Campo, G. Bedoya, Association of IL4R-rs1805016 and IL6R-rs8192284 polymorphisms with clinical dengue in children from Colombian populations. *J. Infect. Public Health* **12**, 43–48 (2019).

59. J.-C. Larroche, *Developmental Pathology of the Neonate* (Excerpta Medica, Amsterdam, New York, 1977), vol. xviii, 525 p.

60. R. S. Lanciotti, O. L. Kosoy, J. J. Laven, J. O. Velez, A. J. Lambert, A. J. Johnson, S. M. Stanfield, M. R. Duffy, Genetic and serologic properties of Zika virus associated with an epidemic, Yap State, Micronesia, 2007. *Emerg. Infect. Dis.* **14**, 1232–1239 (2008).

61. C. A. Schneider, W. S. Rasband, K. W. Eliceiri, NIH image to ImageJ: 25 years of image analysis. *Nat. Methods* **9**, 671–675 (2012).

62. Y. Chen, Q. Yu, C.-B. Xu, A convenient method for quantifying collagen fibers in atherosclerotic lesions by ImageJ software. *Int. J. Clin. Exp. Med.* **10**, 14904–14910 (2017).

63. F. Varghese, A. B. Bukhari, R. Malhotra, A. De, IHC Profiler: An open source plugin for the quantitative evaluation and automated scoring of immunohistochemistry images of human tissue samples. *PLOS ONE* **9**, e96801 (2014).

64. A. Dobin, C. A. Davis, F. Schlesinger, J. Drenkow, C. Zaleski, S. Jha, P. Batut, M. Chaisson, T. R. Gingeras, STAR: Ultrafast universal RNA-seq aligner. *Bioinformatics* **29**, 15–21 (2013).

65. J. Shin, D. A. Berg, Y. Zhu, J. Y. Shin, J. Song, M. A. Bonaguidi, G. Enikolopov, D. W. Nauen, K. M. Christian, G.-l. Ming, H. Song, Single-cell RNA-Seq with waterfall reveals molecular cascades underlying adult neurogenesis. *Cell Stem Cell* **17**, 360–372 (2015).

66. M. I. Love, W. Huber, S. Anders, Moderated estimation of fold change and dispersion for RNA-seq data with DESeq2. *Genome Biol.* **15**, 550 (2014).

67. E. Y. Chen, C. M. Tan, Y. Kou, Q. Duan, Z. Wang, G. V. Meirelles, N. R. Clark, A. Ma'ayan, Enrichr: Interactive and collaborative HTML5 gene list enrichment analysis tool. *BMC Bioinformatics* **14**, 128 (2013).

68. Z. Gu, L. Gu, R. Eils, M. Schlesner, B. Brors, *circlize* Implements and enhances circular visualization in R. *Bioinformatics* **30**, 2811–2812 (2014).

69. A. Lex, N. Gehlenborg, H. Strobelt, R. Vuillemot, H. Pfister, UpSet: Visualization of intersecting sets. *IEEE Trans. Vis. Comput. Graph.* **20**, 1983–1992 (2014).

70. B. Langmead, S. L. Salzberg, Fast gapped-read alignment with Bowtie 2. *Nat. Methods* **9**, 357–359 (2012).

71. A. M. Kenna, M. Hanna, E. Banks, A. Sivachenko, K. Cibulskis, A. Kernytsky, K. Garimella, D. Altshuler, S. Gabriel, M. Daly, M. A. DePristo, The Genome Analysis Toolkit: A MapReduce framework for analyzing next-generation DNA sequencing data. *Genome Res.* **20**, 1297–1303 (2010).

72. M. A. DePristo, E. Banks, R. Poplin, K. V. Garimella, J. R. Maguire, C. Hartl, A. A. Philippakis, G. del Angel, M. A. Rivas, M. Hanna, A. M. Kenna, T. J. Fennell, A. M. Kernytsky, A. Y. Sivachenko, K. Cibulskis, S. B. Gabriel, D. Altshuler, M. J. Daly, A framework for variation discovery and genotyping using next-generation DNA sequencing data. *Nat. Genet.* **43**, 491–498 (2011).

73. G. A. Van der Auwera, M. O. Carneiro, C. Hartl, R. Poplin, G. D. Angel, A. Levy-Moonshine, T. Jordan, K. Shakir, D. Roazen, J. Thibault, E. Banks, K. V. Garimella, D. Altshuler, S. Gabriel, M. A. DePristo, From FastQ data to high confidence variant calls: The Genome Analysis Toolkit best practices pipeline. *Curr. Protoc. Bioinformatics* **43**, 11.10.1–11.10.33 (2013).

74. P. Cingolani, A. Platts, L. L. Wang, M. Coon, T. Nguyen, L. Wang, S. J. Land, X. Lu, D. M. Ruden, A program for annotating and predicting the effects of single nucleotide polymorphisms, SnpEff: SNPs in the genome of Drosophila melanogaster strain w[1118]; iso-2; iso-3. *Fly* **6**, 80–92 (2012).

75. P. Cingolani, V. M. Patel, M. Coon, T. Nguyen, S. J. Land, D. M. Ruden, X. Lu, Using Drosophila melanogaster as a model for genotoxic chemical mutational studies with a new program, SnpSift. *Front. Genet.* **3**, 35 (2012).

76. S. T. Sherry, M.-H. Ward, M. Kholodov, J. Baker, L. Phan, E. M. Smigielski, K. Sirotkin, dbSNP: The NCBI database of genetic variation. *Nucleic Acids Res.* **29**, 308–311 (2001).

77. X. Liu, X. Jian, E. Boerwinkle, dbNSFP: A lightweight database of human nonsynonymous SNPs and their functional predictions. *Hum. Mutat.* **32**, 894–899 (2011).

78. M. S. Naslavsky, G. L. Yamamoto, T. F. de Almeida, S. A. M. Ezquina, D. Y. Sunaga, N. Pho, D. Bozoklian, T. O. M. Sandberg, L. A. Brito, M. Lazar, D. V. Bernardo, E. Amaro Jr., Y. A. O. Duarte, M. L. Lebrão, M. R. Passos-Bueno, M. Zatz, Exomic variants of an elderly cohort of Brazilians in the ABraOM database. *Hum. Mutat.* **38**, 751–763 (2017).

79. K. J. van der Velde, E. N. de Boer, C. C. van Diemen, B. Sikkema-Raddatz, K. M. Abbott, A. Knopperts, L. Franke, R. H. Sijmons, T. J. de Koning, C. Wijmenga, R. J. Sinke, M. A. Swertz, GAVIN: Gene-Aware Variant INterpretation for medical sequencing. *Genome Biol.* **18**, 6 (2017).

80. X. Liu, C. Wu, C. Li, E. Boerwinkle, dbNSFP v3.0: A one-stop database of functional predictions and annotations for human nonsynonymous and splice-site SNVs. *Hum. Mutat.* **37**, 235–241 (2016).

81. J. T. Robinson, H. Thorvaldsdóttir, W. Winckler, M. Guttman, E. S. Lander, G. Getz, J. P. Mesirov, Integrative genomics viewer. *Nat. Biotechnol.* **29**, 24–26 (2011).

82. V. Gorshkov, T. Verano-Braga, F. Kjeldsen, SuperQuant: A data processing approach to increase quantitative proteome coverage. *Anal. Chem.* **87**, 6319–6327 (2015).

83. S. Tyanova, T. Temu, P. Sinitcyn, A. Carlson, M. Y. Hein, T. Geiger, M. Mann, J. Cox, The Perseus computational platform for comprehensive analysis of (prote)omics data. *Nat. Methods* **13**, 731–740 (2016).

84. M. E. Ritchie, B. Phipson, D. Wu, Y. Hu, C. W. Law, W. Shi, G. K. Smyth, limma powers differential expression analyses for RNA-sequencing and microarray studies. *Nucleic Acids Res.* **43**, e47 (2015).

85. J. Xia, M. J. Benner, R. E. W. Hancock, NetworkAnalyst - integrative approaches for protein-protein interaction network analysis and visual exploration. *Nucleic Acids Res.* **42**, W167–W174 (2014).

86. P. Shannon, A. Markiel, O. Ozier, N. S. Baliga, J. T. Wang, D. Ramage, N. Amin, B. Schwikowski, T. Ideker, Cytoscape: A software environment for integrated models of biomolecular interaction networks. *Genome Res.* **13**, 2498–2504 (2003).

Science Signaling

Molecular alterations in the extracellular matrix in the brains of newborns with congenital Zika syndrome

Renato S. Aguiar, Fabio Pohl, Guilherme L. Morais, Fabio C. S. Nogueira, Joseane B. Carvalho, Letícia Guida, Luis W. P. Arge, Adriana Melo, Maria E. L. Moreira, Daniela P. Cunha, Leonardo Gomes, Elyzabeth A. Portari, Erika Velasquez, Rafael D. Melani, Paula Pezzuto, Fernanda L. de Castro, Victor E. V. Geddes, Alexandra L. Gerber, Girlene S. Azevedo, Bruno L. Schamber-Reis, Alessandro L. Gonçalves, Inácio Junqueira-de-Azevedo, Milton Y. Nishiyama Jr., Paulo L. Ho, Alessandra S. Schanoski, Viviane Schuch, Amilcar Tanuri, Leila Chimelli, Zilton F. M. Vasconcelos, Gilberto B. Domont, Ana T. R. Vasconcelos and Helder I. Nakaya

How Zika affects the extracellular matrix

      In some cases, Zika virus (ZIKV) infection during pregnancy leads to a series of severe defects in the fetus collectively known as congenital Zika syndrome (CZS). These include microcephaly, defective neuronal migration, and impaired cortical development. Aguiar *et al.* combined genomic, transcriptomic, and proteomic analyses of blood and postmortem brains and demonstrated that ZIKV-infected neonates showed a reduction in collagen expression and an increase in adhesion factor expression, alterations in the extracellular matrix consistent with the brain defects seen in CZS. Together, these datasets form a useful resource for those investigating the molecular mechanisms underlying CZS in humans.

ARTICLE TOOLS	http://stke.sciencemag.org/content/13/635/eaay6736
SUPPLEMENTARY MATERIALS	http://stke.sciencemag.org/content/suppl/2020/06/05/13.635.eaay6736.DC1
RELATED CONTENT	http://stke.sciencemag.org/content/sigtrans/11/519/eaan3580.full http://stke.sciencemag.org/content/sigtrans/11/535/eaas9332.full http://stke.sciencemag.org/content/sigtrans/12/605/eaaw1347.full
REFERENCES	This article cites 85 articles, 15 of which you can access for free http://stke.sciencemag.org/content/13/635/eaay6736#BIBL
PERMISSIONS	http://www.sciencemag.org/help/reprints-and-permissions

Use of this article is subject to the Terms of Service